Journal of
Materials Chemistry A

ROYAL SOCIETY
OF CHEMISTRY

PAPER

View Article Online
View Journal | View Issue

Check for updates

Cite this: *J. Mater. Chem. A*, 2025, **13**, 40139

Degradation of yttria-stabilized zirconia electrolytes: impact of NiO dissolution with and without phase transformation

Katherine Develos-Bagarinao, *[a] Takuya Yamaguchi, [b] Tomohiro Ishiyama, [b] Takaaki Sakai, [b] Toshiaki Yamaguchi [c] and Haruo Kishimoto *[a]

Received 24th July 2025
Accepted 7th October 2025

DOI: 10.1039/d5ta05977a

rsc.li/materials-a

Solid oxide cells (SOCs) utilized for power generation and hydrogen production *via* electrolysis coupled with renewable energy sources are promising technologies for enabling the transition into a zero-carbon society. To ensure the long-term performance of SOCs under fuel cell and electrolysis operation, elucidating the factors governing degradation of the cell's core components such as the electrodes and electrolytes is crucial to accelerating their practical implementation. In this study, the degradation behavior driven by nickel oxide (NiO) dissolution during co-sintering process used in typical cell preparation is comprehensively investigated for state-of-the-art 8 mol% yttria-stabilized zirconia (8YSZ) electrolytes with Ni-YSZ cermet support. Employing advanced characterization techniques including ^{18}O oxygen isotope exchange technique with high-resolution secondary ion mass spectrometry (SIMS) imaging, micro-Raman spectroscopy, and scanning/transmission electron microscopy (S/TEM), it is revealed that the degradation of oxide ion diffusivity of 8YSZ proceeds *via* two distinct pathways. The first pathway is activated by the instantaneous reduction of NiO to metallic Ni in the 8YSZ bulk, resulting in a drastic drop in oxide ion diffusivity; the second one proceeds with a decay time constant which is dependent on the reduction temperature. For the high-temperature regime of 900 °C, an accelerated and extensive phase transformation of 8YSZ from cubic to tetragonal phase occurs. This is accompanied by a preferential precipitation of metallic Ni both within the bulk and grain boundaries of 8YSZ and a relatively fast degradation of oxide ion diffusivity. On the other hand, for the intermediate-temperature regime of 700 °C, even if there is no obvious phase transformation nor Ni precipitation, a gradual progression of degradation of the oxide ion diffusivity of 8YSZ is nevertheless observed. Understanding these underlying degradation mechanisms provides useful insights into the long-term stability of 8YSZ electrolytes and their impact on the long-term performance of SOCs.

1 Introduction

Society's energy transition from over-reliance on fossil fuels towards adoption of renewable energies and zero-carbon based energy sources will be steered by technologies which are efficient, cost-cutting, and reliable. High-temperature solid oxide cells (SOCs), operated in fuel cell mode to generate power, or electrolysis mode for converting steam and/or carbon dioxide to hydrogen/carbon monoxide syngas, are potential technologies that can significantly contribute to this energy transition. The commercial competitiveness of SOC technologies, however, needs to be further boosted by drastically reducing capital expenditure (CAPEX) and operational expenditure (OPEX). Towards this goal, understanding and mitigating factors affecting degradation of performance in long-term operation are necessary steps to accelerate the widespread implementation of SOC technologies. To date, durability projects on stacks/cells operated in fuel cell mode[1–3] and electrolysis mode[4–6] have revealed a variety of degradation phenomena associated with the core components of the cells, namely electrodes and electrolytes. Interestingly, the accelerated increase in the ohmic resistance has been reported to be the main contributor to the degradation of stacks.[7,8] Ohmic resistance in both fuel cell and electrolysis operation can increase due to various factors, including material degradation,[9] electrolyte conductivity degradation,[1,10,11] and operating conditions.[12–14]

Cubic-stabilized zirconia doped with 8 mol% Y_2O_3 (8YSZ) is a state-of-the-art electrolyte material frequently utilized for SOCs due to its high oxide ionic conductivity, high chemical

---

[a] Global Zero Emission Research Center (GZR), National Institute of Advanced Industrial Science and Technology (AIST), 16-1 Onogawa, Tsukuba, Ibaraki 305-8569, Japan. E-mail: develos-bagarinao@aist.go.jp; haruo-kishimoto@aist.go.jp

[b] Research Institute for Energy Efficient Technology (RIEET), National Institute of Advanced Industrial Science and Technology (AIST), 1-1-1 Higashi, Tsukuba, Ibaraki 305-8565, Japan

[c] Energy Process Research Institute (EPRI), National Institute of Advanced Industrial Science and Technology (AIST), 16-1 Onogawa, Tsukuba, Ibaraki 305-8569, Japan

stability and high mechanical strength.[15–18] To fulfill the requirement for gas tightness and high open circuit voltage (OCV) values, fabrication using conventional processing methods such as screen printing requires sintering at temperatures exceeding 1300 °C in order to obtain dense and pinhole-free 8YSZ layers. Pinhole formation can result in gas leakage and localized temperature increase, leading to low OCV values as well as inaccurate evaluation of performance.[19] For the case of fuel-electrode-supported cells, 8YSZ electrolytes are also typically co-sintered with the NiO-YSZ support at similarly high temperatures. On the other hand, high processing temperatures invariably promote accelerated cation interdiffusion across interfaces and consequently degrade the oxide ion conductivity of 8YSZ.[10,11] Previous studies have indicated that 8YSZ electrolytes intentionally doped with NiO exhibit phase transformation from cubic to tetragonal phase upon reduction in hydrogen atmosphere and is associated with the oxygen potential distribution in the 8YSZ.[10,11,20] Nevertheless, these studies are mostly limited to bulk samples intentionally doped with NiO and other oxide materials. Currently, there is still a lack of systematic investigation of this phenomenon in 8YSZ electrolytes co-sintered with Ni-YSZ-supported cell structures typically utilized in SOCs. Additionally, it is extremely difficult to measure the conductivity of a thin electrolyte, especially one which is in contact with conductive materials such as electrode materials. While NiO dissolution into 8YSZ itself is not a new phenomenon, how the Ni distribution evolves with operating conditions, and the consequences of this behavior on electrolyte properties are still unknown. Elucidating the factors that govern degradation behavior of 8YSZ electrolytes will be indispensable towards the selection of appropriate fabrication conditions to improve the performance and stability of cell components.

Towards the goal of understanding the degradation phenomena occurring in 8YSZ electrolytes used in Ni-YSZ-supported cells, in this study, a systematic investigation of the correlation between NiO dissolution and the stability of 8YSZ electrolytes by varying sintering temperature as well as reduction temperature and time is performed. We examined in detail the impact of NiO dissolution in the 8YSZ electrolytes by visualizing oxide ion transport, Ni distribution and microstructural changes, using a combination of micro-Raman spectroscopy, ^{18}O isotope exchange technique in conjunction with high-resolution secondary ion mass spectrometry (SIMS) imaging, and scanning/transmission electron microscopy (S/TEM), and correlate these results to the often-reported phenomenon of phase transformation of 8YSZ from cubic to tetragonal phase. Given the inherent difficulties in directly evaluating the conductivity (σ) of 8YSZ electrolytes within a typical SOC structure, we employed an alternative approach based on oxide ion diffusivity (D^*), derived from fitting the ^{18}O isotope exchange depth profiles using SIMS. This method enables a more precise assessment of the 8YSZ electrolyte degradation, independent of other factors influencing ohmic resistance and overall cell performance. Moreover, this approach enables a systematic assessment of the impact of NiO dissolution and its correlation with the degradation of the 8YSZ electrolyte. Our findings reveal that there are two distinct pathways that govern the degradation behavior of 8YSZ with dissolved NiO: the first is a fast process activated instantaneously upon the onset of NiO reduction, and the second proceeds with a decay time constant dependent on the temperature of reduction. In the high-temperature regime of 900 °C, where the decay time constant is relatively short, this is accompanied by a rapid drop in oxygen diffusivity due to the phase transformation of 8YSZ from cubic to tetragonal and preferential precipitation of metallic Ni. In the intermediate-temperature regime of 700 °C, where the decay time constant is relatively long, there is neither phase transformation nor Ni precipitation observed, nevertheless, the oxygen diffusivity degradation still gradually progresses with time. These processes are considered to contribute to the observed degradation of the 8YSZ electrolyte conductivity and offer insights into possible mitigation strategies to enhance stability and performance of YSZ-based SOCs.

2 Experimental

2.1 Sample preparation

NiO-YSZ cermet supports were prepared *via* the extrusion method, with NiO-YSZ functional layers (FLs) prepared using the dip-coating method (60 wt% NiO, 40 wt% YSZ) and calcined at 1000 °C for 1 h. 8YSZ electrolytes were subsequently prepared on the NiO-YSZ-supported substrates using the dip-coating method, with sintering performed at 1370 °C, 1450 °C, and 1550 °C for 2 hours each. The final thicknesses obtained were ∼20–30 μm. The samples were then individually reduced at 900 °C and 700 °C under a flow of 50 ccm dry H_2 for various lengths of time ranging from 5, 100, and 300 hours.

2.2 Characterization

Isotope exchange was performed for the samples by pre-annealing first in pure $^{16}O_2$ gas at 400 °C for 14 minutes; afterwards, the atmosphere was abruptly changed to $^{18}O_2$ and the exchange lasted for 10 minutes. The cells were then rapidly quenched to room temperature. Specimens for analyses were prepared by mounting the samples with resin and metal alloy inside holders, then finely polishing the cross-sections. The samples were first analyzed using micro-Raman spectroscopy (JASCO, NR-3100 with 532 nm excitation laser) to detect the phase transformation occurring in the 8YSZ electrolytes. For succeeding microscopy and SIMS analyses, the samples were additionally coated with a thin layer (∼3 nm) of conductive Os coating evaporated at room temperature. The samples were imaged using dual-beam plasma focused ion beam-scanning electron microscopy (pFIB-SEM, Helios 5 Hydra CX, Thermo-Fisher) operated at an acceleration voltage of 5 kV. The measurements were performed across the cross-section of each sample.

The elemental distribution across the cross-sections of the samples was further evaluated using high-resolution SIMS imaging (NanoSIMS 50L, Ametek CAMECA). NanoSIMS measurements were performed using a primary ion beam of Cs^+ accelerated at 8 kV, and simultaneous detection of secondary ions of $^{16}O^-$, $^{18}O^-$, $^{58}Ni^-$, $^{89}Y^{16}O^-$, and $^{94}Zr^{16}O^-$ was conducted using a multicollection system. Raster sizes were varied from 50 μm to 10 μm. The acquired images were processed using WinImage 4.6 (Ametek CAMECA).

Specimens for S/TEM analyses were prepared using pFIB-SEM (Helios 5 Hydra CX, ThermoFisher) using Xe^+ ions accelerated at a maximum voltage of 30 kV, with final thinning to <100 nm performed with Ar^+ ions accelerated at 8 kV. S/TEM (Tecnai Osiris, FEI) analyses were performed at room temperature using a beam acceleration voltage of 200 kV. Energy dispersive X-ray spectroscopy (EDX) was performed using four windowless silicon drift detectors (FEI SuperX) equipped in the S/TEM system.

3 Results and discussion

3.1 Microstructural evolution and phase transformation

Typical cross-sectional SEM backscattered electron images obtained from the various samples in this study are shown in Fig. 1. The top row shows the samples reduced at 700 °C for 100 h, whereas the bottom row shows those reduced at 900 °C for 100 h. Samples sintered at 1370 °C, 1450 °C, and 1550 °C are shown in Fig. 1a–f, respectively. From these results we can extract the following observations: first, all 8YSZ electrolytes exhibit a uniformly dense microstructure with well-connected grains and demonstrate good interfacial contact with their respective Ni-YSZ FLs; secondly, the higher the sintering temperature, the larger the grain sizes of the 8YSZ electrolytes. For the sample sintered at the lowest temperature of 1370 °C, the largest grains have sizes of only a few micrometers; for the sample sintered at the highest temperature of 1550 °C, the largest grains exhibit sizes exceeding 10 μm. Lastly, a similar grain growth can be seen for the FL, wherein relatively larger 8YSZ grains (distinguished by their brighter contrast in comparison to the slightly darker Ni grains) could be observed for samples sintered at higher temperatures. This also results in overall lower porosities especially at the 8YSZ electrolyte-FL interfaces. However, aside from the obvious grain growth it is

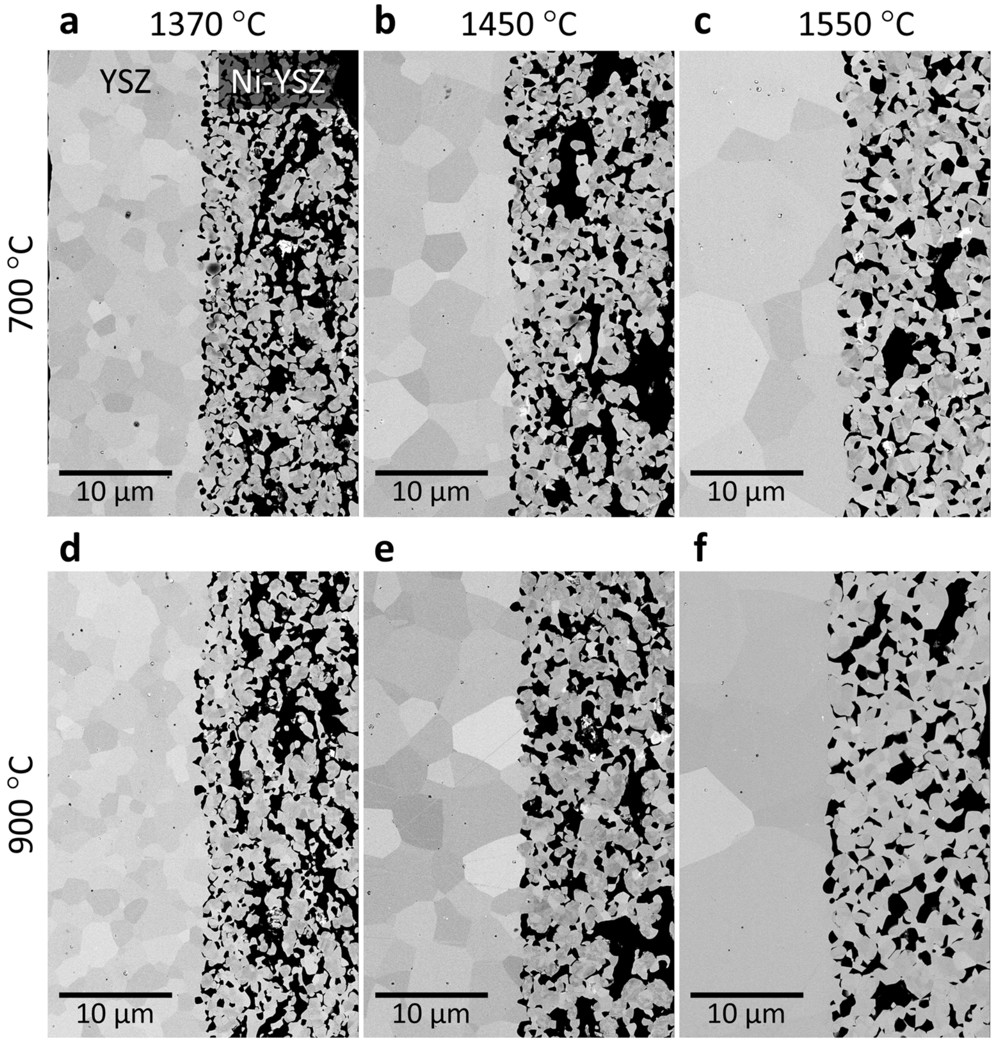

Fig. 1 Typical SEM backscattered electron images of 8YSZ/Ni-YSZ half cells obtained after reducing at 700 °C for 100 h (top row: a–c) and 900 °C for 100 h (bottom row: d–f). (a) and (d): sintered at 1370 °C; (b) and (e): sintered at 1450 °C, and (c) and (f): sintered at 1550 °C.

difficult to ascertain if there are any other microstructural changes. Within the resolution of the SEM instrument there does not seem to be any obvious precipitation nor secondary phase formations at the grain boundaries of the 8YSZ electrolytes. Based solely on morphological features, it is difficult to verify whether there are any indications of electrolyte degradation.

Fig. 2 shows the Raman spectra obtained from the cross-sections of the 8YSZ electrolytes prepared at various conditions. Fig. 2a–c show the Raman spectra for 8YSZ electrolytes sintered at various temperatures of 1370 °C, 1450 °C, and 1550 °C, respectively. The samples reduced at 700 °C for 100 h are depicted by the top spectra shown in blue; the corresponding samples reduced at 900 °C are depicted by the bottom spectra shown in red. Here, the peaks marked with a square (■) are attributed to the cubic phase, whereas those marked with a star (★) are attributed to the tetragonal phase.[1,10,11] There is, however, an overlap of the peaks attributed to the cubic and tetragonal phases occurring at ~610–620 cm^{-1}, rendering quantification of the phases inherently difficult. Regardless of the sintering temperature which influences the amount of diffused NiO in the 8YSZ electrolytes, all samples reduced at 700 °C for 100 h exhibit relatively high stability of the cubic phase of 8YSZ. By contrast, all samples reduced at 900 °C for 100 h exhibit prominent peaks attributable to the tetragonal phase of 8YSZ. Based on these results, the phase transformation of 8YSZ is remarkably accelerated with increased reduction temperature. In addition, as indicated by the Raman spectra for samples sintered at 1450 °C and reduced at 700 °C (Fig. 2d) and 900 °C (Fig. 2e) at various times, 8YSZ electrolytes remain mostly cubic when reduced at a relatively low temperature of 700 °C, but consistently undergo a rapid phase transformation to tetragonal phase at a relatively higher reduction temperature of 900 °C. The peaks attributed to the tetragonal phase, such as the peaks at 255 cm^{-1} and 145 cm^{-1}, are already visible for the sample reduced at 900 °C even at relatively brief time of 5 h (Fig. 2e). The relative intensities of these peaks are also observed to increase with time, indicating the continuous progression of the transformation into the tetragonal phase.

Fig. 3 shows the distribution of Ni as evaluated using NanoSIMS (raster area: 30 μm × 30 μm) for 8YSZ electrolytes sintered at different temperatures and reduced at 700 °C and

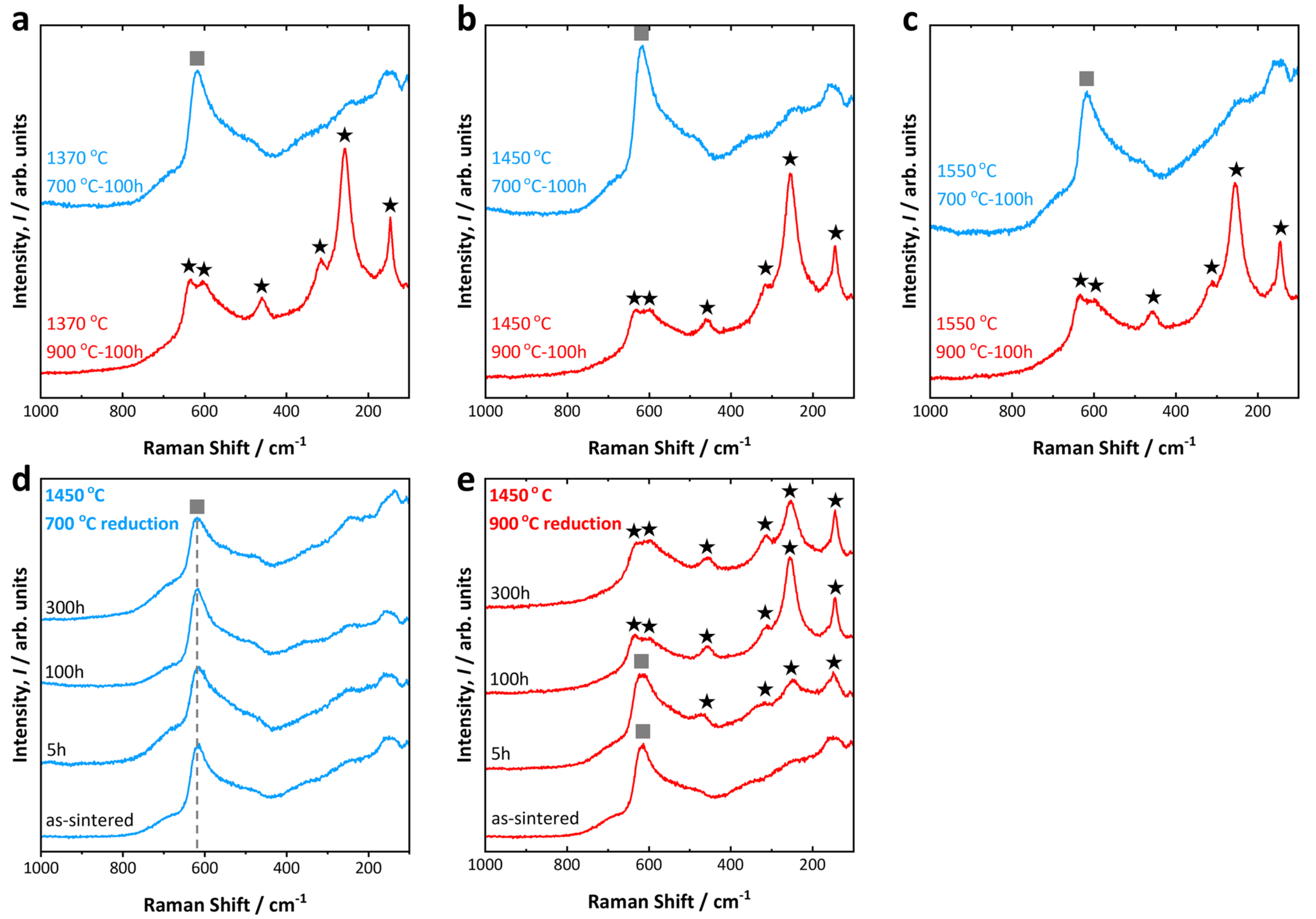

Fig. 2 Raman spectra of 8YSZ electrolytes sintered on Ni-YSZ support: (a) sintered at 1370 °C and reduced at 700 °C for 100 h (top spectra, depicted in blue) and 900 °C for 100 h (bottom spectra, depicted in red); (b) and (c): corresponding spectra for 8YSZ electrolytes sintered at 1450 °C and 1550 °C, respectively; (d) comparison of 8YSZ electrolytes as-sintered at 1450 °C and reduced at 700 °C for various times (5, 100, and 300 h); (e) comparison of 8YSZ electrolytes as-sintered at 1450 °C and reduced at 900 °C for various times (5, 100, and 300 h). Peaks marked with a square (■) are attributed to the cubic phase, whereas those marked with a star (★) are attributed to the tetragonal phase.

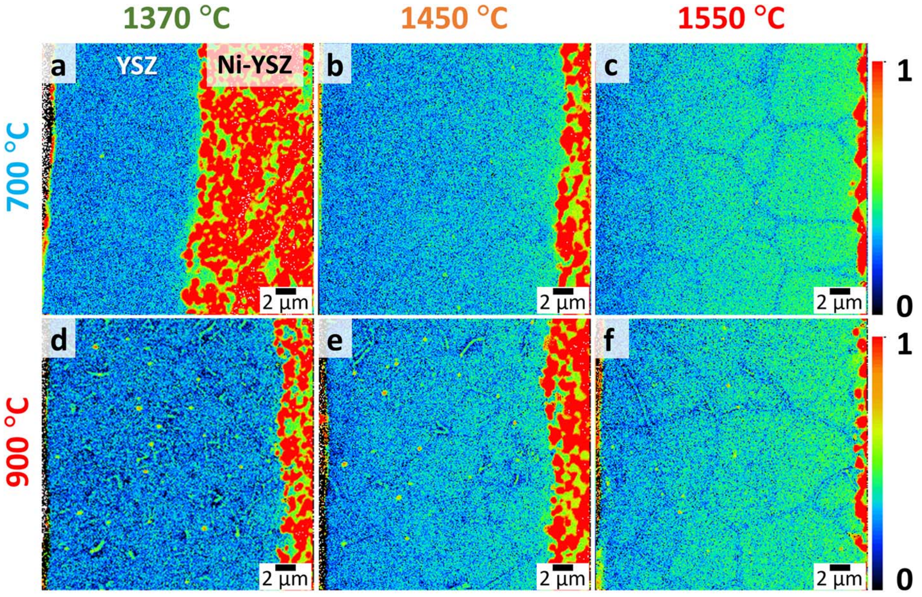

Fig. 3 NanoSIMS images depicting the distribution of Ni ($^{58}Ni^-$ secondary ion intensities normalized by $^{94}Zr^{16}O^-$), for 8YSZ/Ni-YSZ samples sintered at 1370 °C (a and d), 1450 °C (b and e), and 1550 °C (c and f). Samples depicted in the top row (a–c) were reduced at 700 °C for 100 h; those in the bottom row (d–f) were reduced at 900 °C for 100 h. Raster area: 30 μm × 30 μm.

900 °C for 100 h each. Here, the $^{58}Ni^-$ secondary ion intensities are normalized by $^{94}Zr^{16}O^-$ for a semi-quantitative comparison across samples. According to the scale bar shown, red regions correspond to higher concentrations, whereas blue regions correspond to lower concentrations. Samples which were sintered at lower temperatures, *e.g.*, 1370 °C, exhibit relatively lower concentrations of Ni (as depicted by blue-colored regions) whereas those sintered at higher temperatures exhibit higher concentrations of Ni, as depicted by green-colored regions near the vicinity of the Ni-YSZ. The NanoSIMS normalized signals were further used to determine semi-quantitatively the concentration of NiO dissolved in the 8YSZ electrolytes by using reference bulk samples with known concentrations (Fig. S1, SI). Line profiles obtained from the NanoSIMS images shown in Fig. S1b indicate nearly two times higher relative concentration of Ni near the Ni-YSZ for the samples sintered at 1550 °C compared to those sintered at a lower temperature of 1370 °C. The 1550 °C samples, however, exhibit the steepest concentration gradient across the thickness of the 8YSZ electrolyte, *e.g.*, the relative concentration drops by almost 50%. Nevertheless, there are no particular changes in the relative concentration of Ni as a function of reduction temperature or time (Fig. S1c–e). These results indicate that the amount of NiO dissolved into the 8YSZ electrolyte is fully determined during the co-sintering process.[21] The concentration gradient only becomes apparent because of the relatively thick layers used in this study, though this is not likely to be an issue for most 8YSZ electrolytes employed in fuel-electrode-supported cells, which typically have thicknesses in the range of approximately 2 to 5 μm. Furthermore, the degradation of electrical conductivity of 8YSZ electrolyte does not differ significantly at such low concentrations, *i.e.*, the difference between the conductivity degradation behavior of an 8YSZ doped with 1 mol% NiO and one doped with 0.5 mol% NiO is not very significant (Fig. S3, SI).

Interestingly, although a gradient in Ni concentration along the 8YSZ electrolyte thickness is observed, the grain boundaries appear to have relatively lower concentrations of Ni compared to the bulk. On the other hand, irrespective of the sintering temperature, all samples reduced at 900 °C exhibit prominent Ni precipitation at the grain boundaries. Further details can be seen in images acquired at a smaller raster size as shown in Fig. 4 (raster area: 10 μm × 10 μm). A similar behavior has been reported previously by Coors *et al.*, where discrete Ni metallic precipitates were observed in reduced 1 wt%NiO-8YSZ bulk samples.[22] This phenomenon is presumably related to the reduction of Ni in the lattice from Ni^{2+} to Ni^0, resulting in the precipitation of metallic Ni at the grain boundaries of 8YSZ. Further discussion on this mechanism will be presented later. Nevertheless, it is observed that a significant amount of Ni still remains within the 8YSZ bulk, which is most noticeable for the case of the 8YSZ sintered at the highest temperature of 1550 °C (Fig. 4c and f).

Given that the phase transformation seems more strongly influenced by the reduction temperature, we focus more closely on the 8YSZ electrolytes sintered at 1450 °C. Fig. 5 shows the STEM-HAADF (high-angle annular dark-field) images and STEM-EDX mapping for Ni, Zr, and Y obtained for the 8YSZ electrolytes as-sintered at 1450 °C (Fig. 5a) and subsequently reduced at 700 °C for 300 h (Fig. 5b), and 900 °C for 300 h (Fig. 5c). Additional data obtained for the 8YSZ samples reduced at 700 °C for 100 h and 900 °C for 100 h are presented in Fig. S2 (SI). Here, we can observe that the Zr and Y distributions are homogeneous for all samples, suggesting that there is no significant host cation redistribution resulting from the

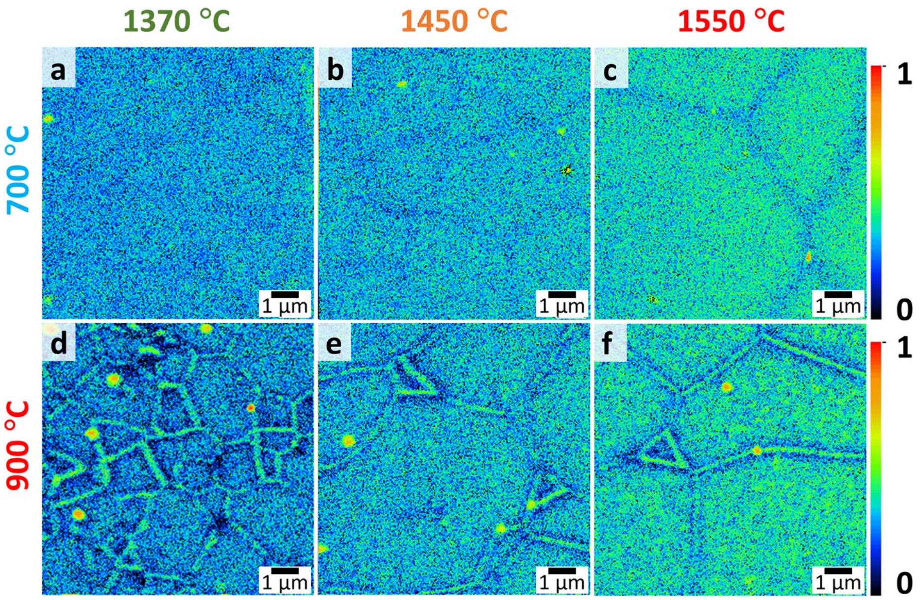

Fig. 4 NanoSIMS images depicting the distribution of Ni (^{58}Ni^{-} secondary ion intensities normalized by ^{94}Zr^{16}O^{-}) within the 8YSZ layers sintered at 1370 °C (a and d), 1450 °C (b and e), and 1550 °C (c and f). Samples depicted in the top row (a–c) were reduced at 700 °C for 100 h; those in the bottom row (d–f) were reduced at 900 °C for 100 h. For samples reduced at 900 °C, preferential precipitation of Ni at the grain boundaries of 8YSZ can be observed. Raster area: 10 µm × 10 µm.

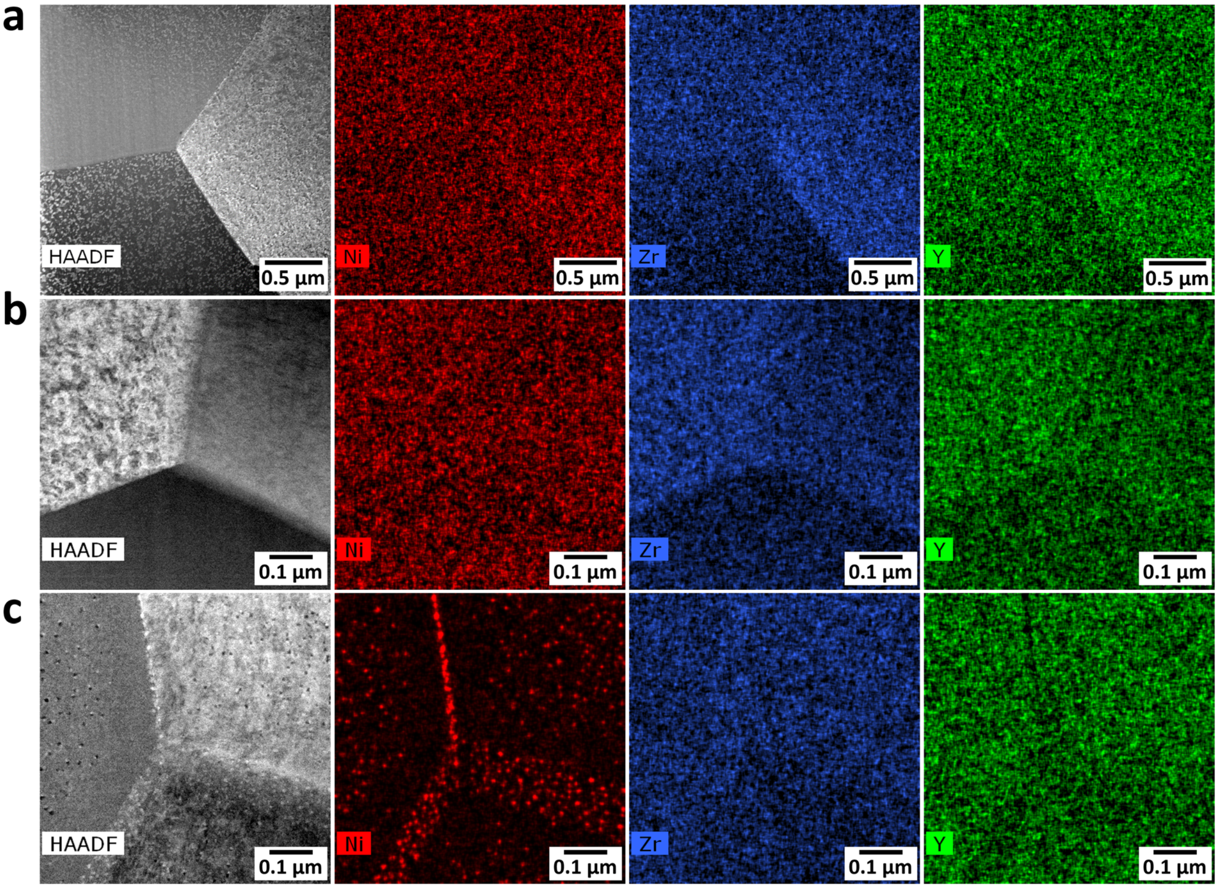

Fig. 5 STEM-HAADF (leftmost panel) and STEM-EDX mapping for Ni, Zr, and Y obtained for 8YSZ electrolytes as-sintered at 1450 °C (a) and subsequently reduced at 700 °C/300 h (b), and 900 °C/300 h (c). The distributions of Zr and Y appear homogeneous for all samples. Unlike samples reduced at 700 °C, those reduced at 900 °C exhibit preferential precipitation of Ni at the grain boundaries and the bulk of 8YSZ.

reduction process. On the other hand, these images reveal a remarkable difference between the 700 °C and 900 °C-reduced 8YSZ in terms of the Ni distribution. In particular, Ni appears homogeneously distributed across the bulk and the grain boundaries of the sample reduced at 700 °C, whereas there is a preferential precipitation of Ni at the grain boundaries and the bulk of the one reduced at 900 °C. These findings are consistent with the NanoSIMS images presented in Fig. 3 and 4. Correlating these results with the Raman spectra, the phase transformation of 8YSZ into tetragonal phase seems to occur simultaneously with the Ni out-diffusion behavior, lending further support to the conclusion that the phase transformation originates from the reduction of the dissolved NiO within the 8YSZ bulk.

Fig. 6 shows the high-magnification STEM-EDX mapping obtained from a region within a grain in the 8YSZ electrolyte reduced at 900 °C for 300 h. Here, we can observe the presence of Ni precipitates adjacent to closed voids in the grain interior. The overlay image of the STEM-HAADF and Ni mapping shows the exact location of the Ni precipitates and their distribution, and the Y and Zr mapping do not indicate any particular inhomogeneities nor correlation with the distribution of either Ni or the closed voids. However, this may be a limitation of the resolution of the instrument used and more advanced analysis with higher resolution in future investigations may be able to provide additional information on the cation distribution at the atomic scale.

Fig. 7 shows a typical selected area electron diffraction (SAED) pattern measured on the 8YSZ electrolyte reduced at 900 °C for 300 h. The strong reflections in Fig. 7a are attributed to the cubic phase of 8YSZ. The SAED pattern also exhibits weak reflections (marked by white circles) forbidden in the 8YSZ cubic fluorite structure; these reflections are ascribed to the tetragonal phase. Following the method described in previous studies, dark-field TEM imaging with a {112} reflection was conducted to evaluate the distribution of the tetragonal phase.[23,24] Fig. 7b shows the bright-field TEM image acquired on a single 8YSZ grain which exhibits several embedded Ni precipitates, similar to the one shown in Fig. 6a. In this image, the Ni precipitates appear within closed voids shown in bright contrast (some examples are marked with black arrows) in the 8YSZ grain interior. The corresponding dark-field TEM image with {112} reflection acquired in the same region of interest is shown in Fig. 7c; regions attributed to the tetragonal phase are shown in bright contrast, whereas those attributed to the cubic phase are shown in dark contrast. Here we can observe that the tetragonal phase regions are comprised of spheroidal particles of ∼10–20 nm in size, and their locations do not necessarily coincide with those of Ni precipitates but appear as randomly distributed nanodomains. While it is difficult to estimate the

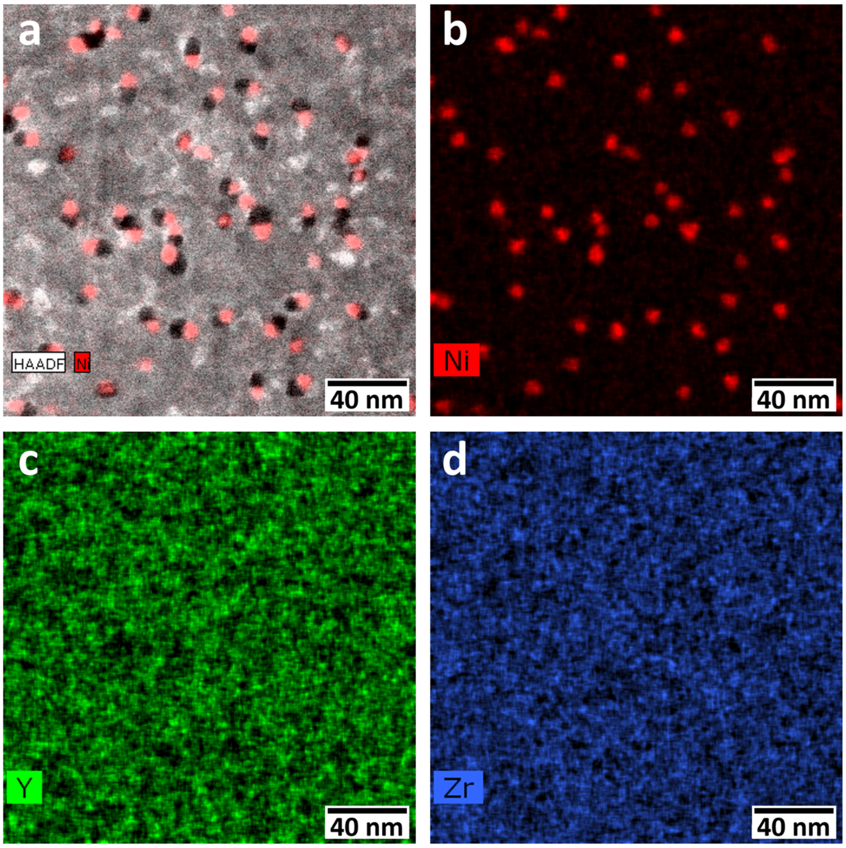

Fig. 6 (a) Overlay of the STEM-HAADF and Ni mapping acquired on a grain of the 8YSZ electrolyte reduced at 900 °C for 300 h. Ni precipitates (depicted in red) are located adjacent to closed voids (black regions) within the grain. (b)–(d) Elemental mapping for Ni, Y, and Zr, respectively, acquired in the same region shown in (a).

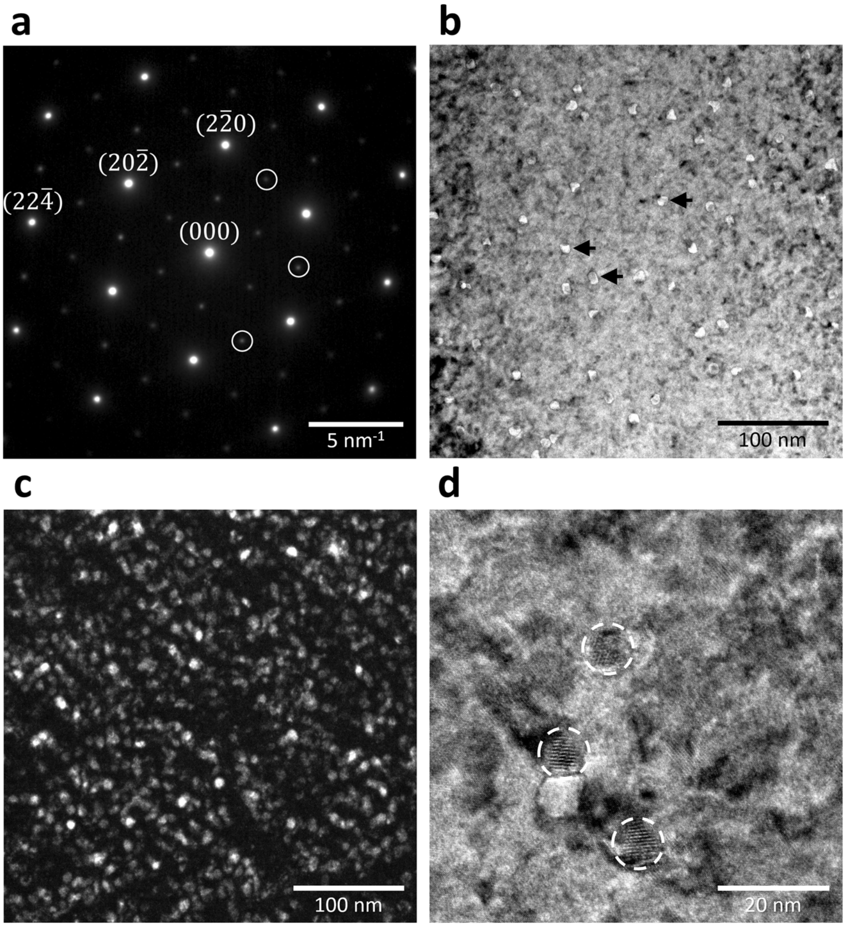

Fig. 7 (a) SAED pattern along the [111]-zone axis of 8YSZ reduced at 900 °C for 300 h. A few locations of diffraction spots forbidden in the cubic fluorite structure are marked by white circles. (b) Bright-field TEM image of a representative region exhibiting Ni precipitates at pore areas. Some examples of pores are marked by black arrows. (c) Corresponding dark-field TEM image acquired with a {112} reflection. Bright-contrast regions are attributed to the tetragonal phase; dark-contrast regions are attributed to the cubic phase. (d) High-magnification TEM image of a representative region; some Ni precipitates embedded in the 8YSZ lattice are indicated by white dashed circles.

percentage of 8YSZ that has transformed to the tetragonal phase, from the TEM image it is clear that the phase transformation progresses with the formation of tetragonal phase nanodomains randomly interspersed with the cubic phase. Lastly, Fig. 7d shows a high-magnification TEM image of a representative region, depicting some Ni precipitates embedded in the 8YSZ bulk (indicated by white dashed circles). The Ni precipitates appear distinct from the 8YSZ lattice and there are no apparent strains or dislocations observed in the vicinity of each precipitate.

Similar SAED and TEM analyses were also performed for the sample reduced at 700 °C and 300 h; the results are presented in Fig. S4, SI. The SAED pattern shown in Fig. S4a displays prominent diffraction spots characteristic of the cubic phase of 8YSZ. While weak, diffuse spots corresponding to the forbidden reflection seem apparent, they are significantly less pronounced than those observed in the 900 °C sample (Fig. 7a), making the assessment of the presence of the tetragonal phase in the sample difficult. Furthermore, representative TEM images in Fig. S4b and c – acquired at the same magnification as Fig. 7d – show no clear evidence of Ni precipitation, either at grain boundaries or within grain interiors. Additional regions examined within the same sample similarly revealed no obvious signs of Ni precipitation. These findings further support the lack of accelerated tetragonal phase formation or obvious Ni precipitation in this sample.

3.2 Evaluation of the diffusion coefficient D^*

Based on the results presented so far, it has been revealed that the features of Ni distribution within the 8YSZ electrolytes are determined by the temperature at which reduction is performed. For long-term SOC operation, it is of high importance to understand how the dissolution and diffusion of Ni contributes to the degradation of the ionic conductivity of 8YSZ. For this purpose, ^{18}O isotope exchange was conducted for each of the samples sintered at 1450 °C and subsequently reduced at 700 °C and 900 °C for various lengths of time. For comparison, an as-sintered sample was also isotopically exchanged under the same conditions. Fig. 8a shows the NanoSIMS images obtained in the vicinity of the 8YSZ/Ni-YSZ interfaces for the

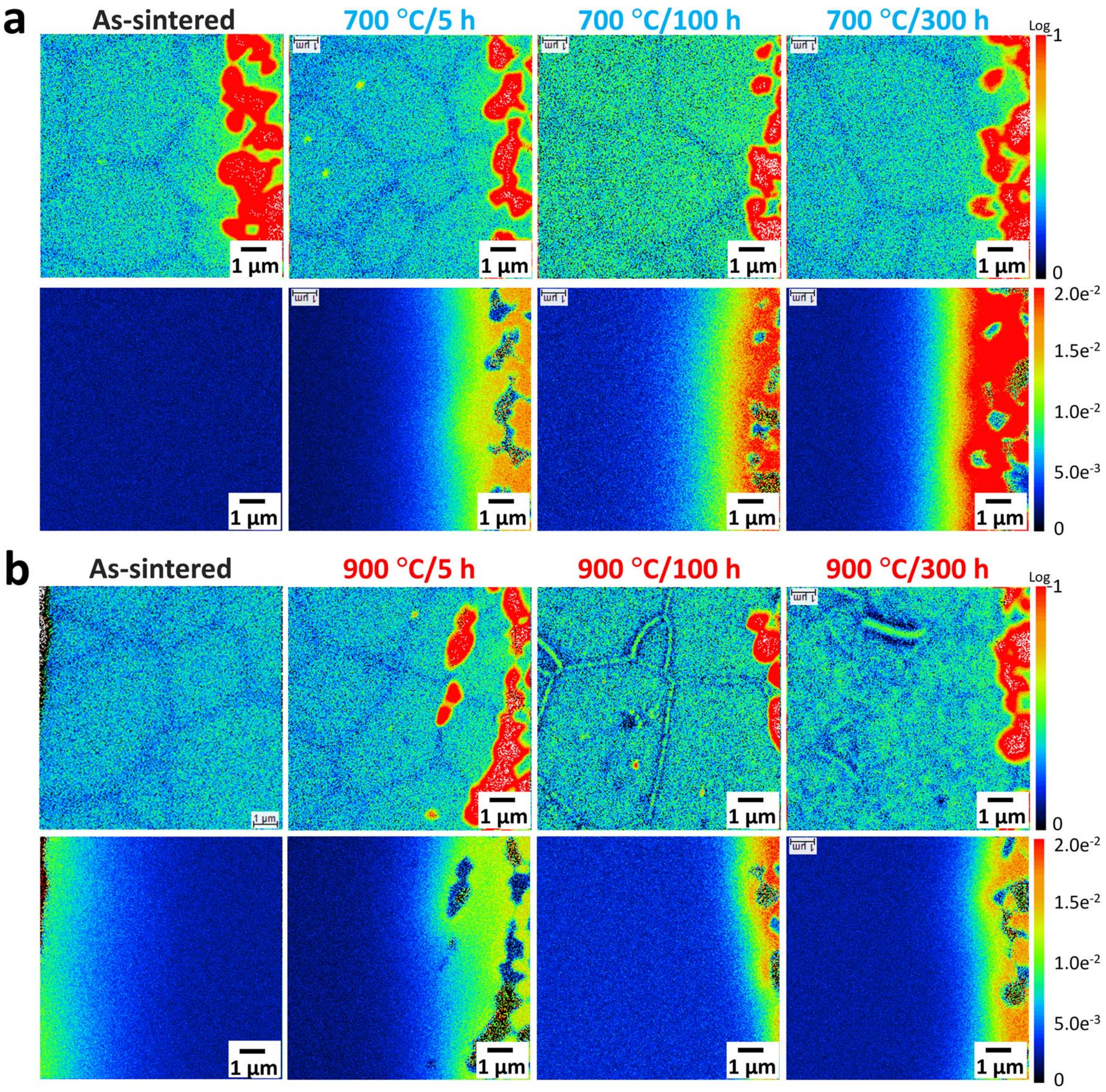

Fig. 8 Top row images: NanoSIMS images depicting the distribution of Ni (normalized by $^{94}Zr^{16}O^-$) for the as-sintered samples and those reduced at 700 °C (a) and 900 °C (b) for various times. Bottom row images: corresponding images depicting the normalized fraction of the ^{18}O isotopic tracer, c_{18O}, given by eqn (1).

samples reduced at 700 °C. The top row depicts the distribution of Ni (normalized intensities), whereas the bottom row depicts the corresponding distribution of the normalized fraction of the $^{18}O^-$ concentration, c_{18O}, expressed by the following equation:

$$c_{18O} = \frac{^{18}O^-}{^{18}O^- + ^{16}O^-} \tag{1}$$

where $^{18}O^-$ and $^{16}O^-$ are the secondary ion intensities measured using NanoSIMS. As can be seen in Fig. 8a, for the as-sintered 8YSZ there is no detectable $^{18}O^-$ tracer incorporated from the oxygen isotope exchange, which is as expected due to the absence of pores in the NiO-YSZ support structure for gas diffusion. On the other hand, gradients in c_{18O} distribution can be clearly observed across the layers of the H_2-reduced samples. Here, high concentrations of ^{18}O are observed for the Ni-YSZ regions (shown in orange or red in the mapping); towards the 8YSZ region, however, we can observe a noticeable decrease in the c_{18O}. Fig. 8b shows the corresponding images for the samples reduced at 900 °C. Here, the analyzed region of the as-sintered sample shown corresponds to the area near its surface, where a thin layer of Pt was applied as an active electrode. This is to facilitate the isotope exchange on the as-sintered 8YSZ electrolyte and obtain a similar ^{18}O diffusion profile. Like the 700 °C samples, those reduced at 900 °C similarly show relatively high concentrations of c_{18O} near the 8YSZ/Ni-YSZ interfaces and exhibit a sharp decrease heading towards the 8YSZ electrolyte region.

To quantitatively analyze the diffusion profiles of c_{18O}, line scan analyses were performed for each of the samples as shown in Fig. 9. An example of a line scan analysis is shown by the inset image, where the analyzed region is defined by an arrow starting from the Ni-YSZ region and extending into the 8YSZ electrolyte.

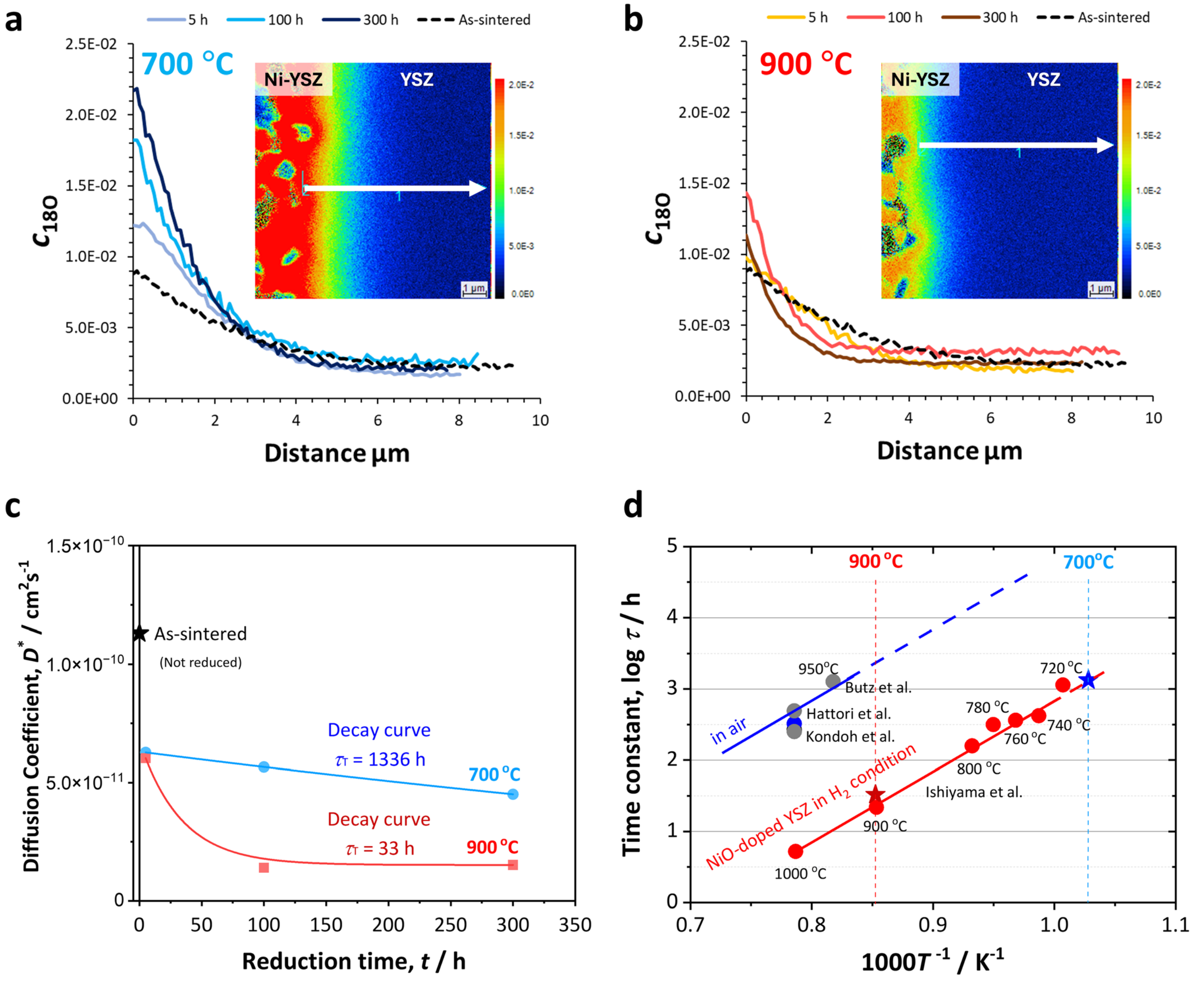

Fig. 9 Profiles of the normalized fraction of the ^{18}O isotopic tracer, c_{18O} for samples reduced at 700 °C (a) and 900 °C (b). Respective insets show examples of line scan analysis performed for each sample. The line profile for the as-sintered sample was obtained at the surface of the 8YSZ layer in contact with Pt electrode. (c) Diffusion coefficient, D^* as a function of reduction time. The time constants are obtained from the fitting of the data with the decay curve equation shown in eqn (3). (d) Arrhenius plot of the decay time constants, τ_T derived for undoped 8YSZ and NiO-doped 8YSZ electrolytes as reported in literature.[26–29] Data obtained in this study (indicated by red and blue stars) are collinear with data reported in literature for NiO-doped 8YSZ annealed in H_2 atmosphere (depicted with a red line).

In Fig. 9a, we can observe that compared to the as-sintered sample, those reduced at 700 °C exhibit a monotonic increase of c_{18O} with longer reduction time, however, the concentration profiles eventually converge at distances greater than ~3 µm and finally level off to the natural abundance concentration of ^{18}O ($c_{18O} = 0.002$). For the samples reduced at 900 °C (Fig. 9b), not only are the c_{18O} values relatively lower than those for 700 °C, but the profiles also exhibit a more drastic decrease within relatively shorter distances.

To evaluate the diffusion coefficient D^*, we adopted the conventional analysis for the interaction of a gas phase with a solid surface, using Crank's solution to the diffusion equation for a semi-infinite medium with a first-order surface exchange limitation[16,25] given by:

$$c_{18O} = \left(C_{bg} + (C_g - C_{bg})\left(\operatorname{erfc}\left(\frac{x}{2\sqrt{D^* t}}\right) - \left[\exp\left(\frac{k^* x}{D^*} + \frac{k^{*2} t}{D^*}\right)\operatorname{erfc}\left(\frac{x}{2\sqrt{D^* t}} + k^*\sqrt{\frac{t}{D^*}}\right)\right]\right)\right) \quad (2)$$

where k^* is the oxygen surface exchange coefficient, C_{bg} is the relative isotopic abundance of ^{18}O ($C_{bg} = 0.002$), C_g is the partial pressure of oxygen ($C_g = 1$), x is the depth, and t is the sample annealing time in $^{18}O_2$ atmosphere.

The extracted diffusion coefficients are plotted as a function of reduction time in Fig. 9c. It is worth noting that the D^* of the reduced samples at a relatively short time of 5 h are already about 40% lower compared to that of the as-sintered sample.

This indicates a rapid degradation in the ionic diffusivity occurring instantaneously from the onset of NiO reduction.

The obtained data were then fitted using a decay curve given as follows:

$$D^* = D_0^* + A_{\mathrm{T}} \exp\left(-\frac{(t-t_0)}{\tau_{\mathrm{T}}}\right) \tag{3}$$

where D_0^* is the diffusion coefficient at an initial time of $t_0 = 5$, A_{T} is a dimensionless fitting parameter, and τ_{T} is the time constant for the decay curve. From the fitting, τ_{T} is calculated to be 1336 h and 33 h for the samples reduced at 700 °C and 900 °C, respectively. In other words, in comparison to the samples reduced at 700 °C, theoretically the degradation is about 40 times accelerated for the case of samples reduced at 900 °C.

D^* is directly proportional to conductivity, σ, through the following equation:

$$\sigma = \frac{Nq^2D^*}{K_{\mathrm{B}}T} \tag{4}$$

where N is the concentration of charge carriers, q is the charge number, K_{B} is the Boltzmann constant, and T is temperature. Therefore, we can assume that the degradation of σ is directly proportional to the degradation of D^*, and the decay time constants can be directly compared. In Fig. 9d, the decay time constants obtained for the conductivities of undoped 8YSZ annealed in air and NiO-doped 8YSZ annealed in H_2 atmosphere as reported in literature are shown in an Arrhenius-type plot.[26–29] The decay time constants for the undoped 8YSZ samples are approximately two orders of magnitude higher than those of NiO-doped 8YSZ, but both plots can be fitted by lines with approximately equivalent slopes. This suggests that the degradation behavior is comparable for both undoped 8YSZ and NiO-doped 8YSZ; the only difference being that the degradation is more accelerated for the latter. This strongly suggests that the presence of NiO itself in the 8YSZ lattice greatly accelerates the degradation of conductivity. The decay time constants τ_{T} obtained in this study are shown in Fig. 9d by blue and red stars for the samples reduced at 700 °C ($\tau_{\mathrm{T}} = 1336$ h) and 900 °C ($\tau_{\mathrm{T}} = 33$ h), respectively. The present data are collinear with the data reported for NiO-doped bulk 8YSZ samples reduced in H_2, suggesting that the oxide ion diffusivity degradation behavior is similar for both 8YSZ electrolytes sintered on Ni-YSZ support and bulk 8YSZ samples intentionally doped with NiO.

From these results it can be inferred that there are at least two pathways for the progression of degradation behavior of NiO-dissolved 8YSZ. The first pathway is a rapid degradation process featuring a sharp drop in oxide ion diffusivity by as much as approximately 40% from the onset of reduction (*i.e.*, at $t = 0$ to $\sim$5 h). This reaches an inflection point which marks the onset of the second pathway, at which the degradation either proceeds at an approximately similar accelerated rate (high-temperature regime, short decay time constant) or a much slower rate (intermediate-temperature regime, long decay time constant). During the accelerated-rate process, the phase transformation from cubic to tetragonal phase is induced, and the oxide ion diffusivity degrades further by about 60% and saturates at this level. On the other hand, for the slower-rate process, such phase transformation behavior could not be detected within the same length of time, owing to the significantly longer time it would require attaining the same levels as with the accelerated condition.

3.3 Mechanisms governing the degradation of oxide ion diffusivity of 8YSZ

NiO dissolution into the 8YSZ lattice is known to decrease the initial ionic conductivity of as-sintered samples; for instance, with the incorporation of 1.5 mol% NiO content in 8YSZ, its conductivity has been reported to decrease by as much as 20% in air. When the atmosphere was changed from air/H_2O to N_2/H_2/H_2O, however, a drastic reduction in conductivity is further exhibited by NiO-doped 8YSZ samples annealed at 1000 °C.[24] When the reduction temperature is in the range of 900 °C and above, this results in a phase transformation from cubic to tetragonal, accompanied by Ni precipitation.[22–24,28] The reported behavior aligns well with that observed in the present study for the 8YSZ samples which were reduced at a higher temperature of 900 °C. However, as we have seen in the preceding results, when the reduction temperature is at an intermediate value of 700 °C, a gradual decrease in conductivity is still evident despite being unable to confirm the occurrence of phase transformation nor Ni precipitation in the 8YSZ samples. This temperature regime is of particular interest, considering that typical SOC devices are normally operated at these intermediate temperatures.

NiO dissolution in the 8YSZ lattice is considered to stabilize the cubic phase from the generation of oxygen vacancies, as described by the following defect reaction (in Kröger–Vink notation):[10,30,31]

$$\mathrm{NiO} \xrightarrow[\mathrm{YSZ}]{} \mathrm{Ni}_{\mathrm{Zr}}'' + \mathrm{V}_{\mathrm{O}}^{\cdot\cdot} + \mathrm{O}_{\mathrm{O}}^{\times} \tag{5}$$

Upon subsequent reduction of NiO in H_2 atmosphere, zerovalent Ni forms in the 8YSZ lattice while also generating oxygen vacancies, as follows:

$$\mathrm{Ni}_{\mathrm{Zr}}'' + \mathrm{O}_{\mathrm{O}}^{\times} \rightarrow \mathrm{Ni}_{\mathrm{Zr}}'''' + \mathrm{V}_{\mathrm{O}}^{\cdot\cdot} + \frac{1}{2}\mathrm{O}_2 \tag{6}$$

Here, $\mathrm{V}_{\mathrm{O}}^{\cdot\cdot}$ (including those already present initially) will strongly interact with the formed zerovalent Ni due to its large Coulomb force. This will result in oxygen vacancy localization[32] or oxygen vacancy ordering which will induce some displacements of cations in 8YSZ, for instance leading to significant enrichment of Y atoms within individual grains.[33] This mechanism likely governs the degradation behavior for the first pathway characterized by a rapid drop in oxygen diffusivity at the onset of reduction.

As mentioned earlier, the subsequent degradation behavior upon prolonged reduction then reaches an inflection point, and from here on the progression will be highly dependent on the reduction temperature. This is because cation diffusion within the 8YSZ lattice is expected to be much faster in the high-temperature regime in comparison to that in the intermediate-temperature regime. SIMS studies on Zr and Ni diffusion in YSZ revealed that their diffusion coefficients increase by approximately one order of magnitude when the temperature is increased by 100 °C.[34,35] In other words, theoretically we could expect a difference of about two orders of magnitude for the cation diffusivities between 8YSZ samples reduced at 700 °C and 900 °C. Moreover, it has been reported that the activation enthalpy (ΔH) of 3.8 ± 0.3 eV for Ni diffusion in YSZ is lower by 1–2 eV compared to the host cations' (Y and Zr) diffusion.[35] This suggests that Ni diffusion is more thermodynamically favorable compared to either Y or Zr and therefore plays a more critical role in determining the degradation behavior of 8YSZ.

The formation of zerovalent Ni is also considered to lead to the creation of vacant Zr^{4+} sites accompanied by defect clusters described by Morrissey *et al.*, as follows:[31]

$$\mathrm{Ni}_{\mathrm{Zr}}'' + 2\mathrm{e}_{\mathrm{gb}}' + \mathrm{V}_{\mathrm{O}}^{\cdot\cdot} \leftrightarrow \mathrm{Ni}_{\mathrm{gb}}^{0} + \left(\mathrm{V}_{\mathrm{Zr}}'''' + \mathrm{V}_{\mathrm{O}}^{\cdot\cdot}\right)'' \tag{7}$$

where $(\mathrm{V}_{\mathrm{Zr}}'''' + \mathrm{V}_{\mathrm{O}}^{\cdot\cdot})''$ refers to the defect cluster, and $\mathrm{Ni}_{\mathrm{gb}}^{0}$ is the metallic Ni preferentially formed at the grain boundary sites. In this case, the preferential precipitation of metallic Ni at grain boundaries is likely promoted by a higher availability of oxygen vacancies at these sites.[36,37] Due to the Ni diffusion, cation vacancies are consequently generated within the 8YSZ lattice, leading to cation rearrangement or local lattice distortion.[38] This is a plausible scenario given that $\mathrm{V}_{\mathrm{Zr}}''''$ are identified as the most probable point defects responsible for Zr diffusion as suggested by tracer diffusion experiments.[34] When this lattice rearrangement or distortion occurs over a sufficiently wide range, it can then be detected using Raman spectroscopy as tetragonal phase transformation. This corresponds with the region of cation-diffusionless phase transition as described by Yashima *et al.*, where phase decomposition of YSZ into a cubic and tetragonal two-phase coexisting region at intermediate temperatures occurs.[39] Later studies by Yokokawa *et al.* also conjectured that a coherent tetragonal phase (*t*'' or tetragonal symmetry domains) coexists with the cubic phase due to the Y-diffusion in the intermediate temperature regime where slow NiO reduction occurs.[20] This metastable phase could not be distinguished from a cubic phase using usual X-ray diffraction analysis because its cell parameters ratio is equal to unity.[40] Raman spectroscopy, on the other hand, is highly sensitive to distortion of oxide ions, enabling detection of such metastable tetragonal phases.[10]

With longer reduction time, zerovalent Ni formed within the 8YSZ grain interior will eventually precipitate inside closed voids as well. This may be described by a reaction where more vacant Zr^{4+} sites are created:[31]

$$\left(\mathrm{V}_{\mathrm{Zr}}'''' + \mathrm{V}_{\mathrm{O}}^{\cdot\cdot}\right)'' + \mathrm{Ni}_{\mathrm{Zr}}'' + 2\mathrm{e}' + \mathrm{V}_{\mathrm{O}}^{\cdot\cdot} \leftrightarrow \mathrm{Ni}^{0} + \mathrm{V}_{\mathrm{Zr}}'''' + \left(\mathrm{V}_{\mathrm{Zr}}'''' + 2\mathrm{V}_{\mathrm{O}}^{\cdot\cdot}\right)^{\times} \tag{8}$$

where Ni^0 refers to the metallic Ni formed in the vicinity of 8YSZ voids. Here, the cumulative loss of Zr sites could satisfactorily account for the void formation accompanying the precipitation of the metallic Ni particles within the 8YSZ grain interior. As proposed by Morrissey *et al.*,[31] a plausible explanation is that this process is effectively activated only where a critical concentration of vacancy clusters that serve as nucleation sites for Ni^0 is attained. As a case in point, a comparison of the Ni mapping for the 8YSZ samples reduced at 900 °C for 100 h and 300 h shows a much higher density of Ni precipitates within the grain interior of the latter, indicating the proliferation of Ni nucleation sites with longer reduction time. This is further corroborated by the observation of a precipitate-free zone of ~100 nm adjacent to either side of the grain boundaries, see for example the Ni mapping depicted in Fig. 5c. This precipitate-free zone could not be accounted for by a calculated diffusion distance for Ni^{2+} as predicted by Fick's laws and is likely to be due to the relative absence here of oxygen vacancies required for nucleation.

When the temperature is sufficiently high, *i.e.*, in the range of 900 °C and above, these processes occur relatively fast, resulting in a phase transformation and dramatic decrease in oxide ion diffusivity within a relatively brief period of time. Analysis of the sample reduced at 900 °C for 5 h reveals early signs of tetragonal phase formation in the Raman spectra (Fig. 2). Nonetheless, NanoSIMS analysis of the same sample shows no evidence of Ni precipitation at this stage (Fig. 8). Ni precipitation was subsequently confirmed in the sample reduced for 100 h, where the Raman spectra also exhibited more pronounced tetragonal phase peaks, indicating progression of the phase transformation over time. These observations suggest that both tetragonal phase transformation and Ni precipitation are driven by the reduction of NiO to Ni and its subsequent diffusion out of the YSZ lattice. Thus, the relationship between Ni precipitation and phase transformation is not causal, but rather correlative – both are outcomes of the same underlying mechanism. By contrast, at intermediate temperatures for operating SOCs, *viz.*, 700–750 °C, cation diffusion will be comparatively slower and therefore these processes would take a significantly longer time to advance. Within the limits of our study, no phase transformation could be observed for the 8YSZ samples reduced at 700 °C for up to 300 h. In future studies, it would be instructive to confirm if similar behavior could be observed over significantly longer time scales, *e.g.* in the order of 10 000 hours or more. Furthermore, future investigations incorporating numerical computations – such as atomistic simulations – and empirical observations would provide robust support for the proposed defect mechanism. Specifically, advanced techniques like atom probe tomography (APT) could be employed to visualize or quantify vacancy localization and ordering, as well as the associated yttrium enrichment, thereby complementing and strengthening the current findings.

In summary, the oxide ion diffusivity of 8YSZ with dissolved NiO could therefore be expected to degrade progressively with time at a rate much faster compared to that of pure 8YSZ. The rate of this progression is influenced largely by the operating temperature. This could partially account for the commonly observed degradation of the cell's ohmic resistance under long-term operation of SOCs.

4 Conclusions

Due to the widespread use of Ni-YSZ as fuel electrodes in SOCs, the dissolution of NiO into 8YSZ electrolytes is a common occurrence during high-temperature co-sintering. In this study, the impact of NiO dissolution in 8YSZ electrolytes was investigated through advanced characterization techniques, revealing changes in oxide ion transport, Ni distribution, and microstructure. Given the limitations of direct conductivity measurements in SOC structures, oxide ion diffusivity derived from ^{18}O isotope exchange depth profiling was employed, providing empirical evidence of electrolyte degradation, and thereby clarifying its contribution to the degradation of cell performance. It is further revealed that the degradation of oxide ion diffusivity of 8YSZ proceeds *via* distinct pathways. The first pathway instantaneously occurs from the onset of reduction, characterized by a fast degradation process whereby NiO is reduced to zerovalent Ni in the 8YSZ bulk. With prolonged reduction, the second pathway will then progress at a time scale commensurate with the reduction temperature: the higher the reduction temperature, the faster the progression of degradation. For the high-temperature regime of 900 °C, a rapid and extensive phase transformation of 8YSZ from cubic to tetragonal phase and preferential precipitation of metallic Ni both within grain boundaries and closed voids in the grain interior of 8YSZ are observed. This results in further drastic reduction in oxide ion diffusivity. On the other hand, for the intermediate-temperature regime of 700 °C, no apparent phase transformation nor Ni precipitation could be confirmed within the same length of time; nevertheless, a progressive degradation of the oxide ion diffusivity of 8YSZ is observed. Hence, even without any apparent phase transformation, there is still a gradual decrease in ionic conductivity triggered by the NiO reduction within the 8YSZ lattice. This is especially relevant for SOCs which are normally operated at intermediate temperatures of 700–750 °C. To prevent or minimize the electrolyte degradation in long-term operation, it is thus necessary to mitigate the NiO dissolution into the 8YSZ electrolyte during cell processing. One possible solution is to entirely avoid the high-temperature sintering used for conventional cell processing and employ low-temperature physical vapor deposition processes like pulsed laser deposition, sputtering, *etc.*[41–43] Whilst these methods may raise CAPEX due to the inherent complexities in the required equipment (*e.g.*, high-vacuum systems), mitigation of the electrolyte degradation behavior is nevertheless expected to offset total costs by lowering OPEX due to improved cell performance and stability. Another solution is to utilize zirconia compositions which are more stable for prolonged operation, *e.g.*, Y_2O_3 content above 8 mol%.[44] Understanding these underlying mechanisms provides useful insights into the long-term stability of 8YSZ electrolytes and their impact on the long-term performance of SOCs.

Conflicts of interest

There are no conflicts to declare.

Data availability

The data that support the findings of this study are available from the corresponding author upon reasonable request.

Additional data supporting this article have been included as part of the supplementary information (SI): calibration of NiO concentration based on SIMS data; STEM-HAADF and STEM-EDX mapping for samples reduced for 100 h; dependence of 8YSZ conductivity on NiO doping; SAED and TEM images for 8YSZ reduced at 700 °C for 300 h. See DOI: **https://doi.org/10.1039/d5ta05977a**.

Acknowledgements

The authors are grateful to Q. Bai (AIST) for assistance in the sample preparation and preliminary data collection, M. Sanbu (AIST) for TEM specimen preparation and N. Saito (AIST) for technical support in the S/TEM measurements.

References

1 H. Yokokawa, M. Suzuki, M. Yoda, T. Suto, K. Tomida, K. Hiwatashi, M. Shimazu, A. Kawakami, H. Sumi, M. Ohmori, T. Ryu, N. Mori, M. Iha, S. Yatsuzuka, K. Yamaji, H. Kishimoto, K. Develos-Bagarinao, T. Shimonosono, K. Sasaki, S. Taniguchi, T. Kawada, M. Muramatsu, K. Terada, K. Eguchi, T. Matsui, H. Iwai, M. Kishimoto, N. Shikazono, Y. Mugikura, T. Yamamoto, M. Yoshikawa, K. Yasumoto, K. Asano, Y. Matsuzaki, K. Sato and T. Somekawa, *Fuel Cells*, 2019, **19**, 311–339.

2 H. Yokokawa, Y. Hori, T. Shigehisa, M. Suzuki, S. Inoue, T. Suto, K. Tomida, M. Shimazu, A. Kawakami, H. Sumi, M. Ohmori, N. Mori, T. Iha, K. Yamaji, H. Kishimoto, K. Develos-Bagarinao, K. Sasaki, S. Taniguchi, T. Kawada, M. Muramatsu, K. Terada, K. Eguchi, T. Matsui, H. Iwai, M. Kishimoto, N. Shikazono, Y. Mugikura, T. Yamamoto, M. Yoshikawa, K. Yasumoto, K. Asano, Y. Matsuzaki, S. Amaha and T. Somekawa, *Fuel Cells*, 2017, **17**, 473–497.

3 N. H. Menzler, D. Sebold, Y. J. Sohn and S. Zischke, *J. Power Sources*, 2020, **478**, 228770.

4 V. Bilalis, X. Sun, H. L. Frandsen and M. Chen, *J. Power Sources*, 2024, **606**, 234490.

5 F. Tietz, D. Sebold, A. Brisse and J. Schefold, *J. Power Sources*, 2013, **223**, 129–135.

6 X. Sun, P. V. Hendriksen, M. B. Mogensen and M. Chen, *Fuel Cells*, 2019, **19**, 740–747.

7 M. Lang, S. Raab, M. S. Lemcke, C. Bohn and M. Pysik, *Fuel Cells*, 2020, **20**, 690–700.

8 M. Lang, Y. Lee, I. Lee, P. Szabo, J. Hong, J. Cho and R. Costa, *Appl. Energy*, 2025, **386**, 125565.

9 S. Zarabi Golkhatmi, M. I. Asghar and P. D. Lund, *Renew. Sustain. Energy Rev.*, 2022, **161**, 112339.

10 H. Kishimoto, K. Yashiro, T. Shimonosono, M. E. Brito, K. Yamaji, T. Horita, H. Yokokawa and J. Mizusaki, *Electrochim. Acta*, 2012, **82**, 263–267.

11 T. Shimonosono, H. Kishimoto, M. E. Brito, K. Yamaji, T. Horita and H. Yokokawa, *Solid State Ionics*, 2012, **225**, 69–72.

12 F. Monaco, D. Ferreira-Sanchez, M. Hubert, B. Morel, D. Montinaro, D. Grolimund and J. Laurencin, *Int. J. Hydrogen Energy*, 2021, **46**, 31533–31549.

13 G. Sassone, O. Celikbilek, M. Hubert, K. Develos-Bagarinao, T. David, L. Guetaz, I. Martin, J. Villanova, A. Benayad, L. Rorato, J. Vulliet, B. Morel, A. Léon and J. Laurencin, *J. Power Sources*, 2024, **605**, 234541.

14 G. Sassone, O. Celikbilek, M. Hubert, K. Develos-Bagarinao, A. Benayad, B. Morel, A. Léon and J. Laurencin, *J. Electrochem. Soc.*, 2024, **171**, 124507.

15 M. Morales, J. J. Roa, X. G. Capdevila, M. Segarra and S. Pinol, *Acta Mater.*, 2010, **58**, 2504–2509.

16 P. S. Manning, J. D. Sirman and J. A. Kilner, *Solid State Ionics*, 1996, **93**, 125–132.

17 M. Mori, T. Abe, H. Itoh, O. Yamamoto, Y. Takeda and T. Kawahara, *Solid State Ionics*, 1994, **74**, 157–164.

18 J. W. Fergus, *J. Power Sources*, 2006, **162**, 30–40.

19 K. Kumada, K. Sato, T. Kawada, H. Sumi, H. Shimada and T. Hashida, *Fuel Cells*, 2021, **21**, 398–407.

20 H. Yokokawa, H. Kishimoto, T. Shimonosono, K. Yamaji, M. Muramatsu, K. Terada, K. Yashiro and T. Kawada, *J. Electrochem. Energy Convers. Storage*, 2017, **14**, 1–19.

21 Q. Bai, K. D. Bagarinao, T. Ishiyama, T. Yamaguchi and H. Kishimoto, *ECS Trans.*, 2023, **112**, 23–28.

22 W. G. Coors, J. R. O'Brien and J. T. White, *Solid State Ionics*, 2009, **180**, 246–251.

23 B. Butz, R. Schneider, D. Gerthsen, M. Schowalter and A. Rosenauer, *Acta Mater.*, 2009, **57**, 5480–5490.

24 S. Linderoth, N. Bonanos, K. V. Jensen and J. B. Bilde-Sørensen, *J. Am. Ceram. Soc.*, 2001, **84**, 2652–2656.

25 J. Crank, *The Mathematics of Diffusion*, Oxford University Press, London, 2nd edn, 1975.

26 J. Kondoh, T. Kawashima, S. Kikuchi, Y. Tomii and Y. Ito, *J. Electrochem. Soc.*, 1998, **145**, 1527–1536.

27 M. Hattori, Y. Takeda, Y. Sakaki, A. Nakanishi, S. Ohara, K. Mukai, J. H. Lee and T. Fukui, *J. Power Sources*, 2004, **126**, 23–27.

28 B. Butz, P. Kruse, H. Stormer, D. Gerthsen, A. Muller, A. Weber and E. Ivers-Tiffée, *Solid State Ionics*, 2006, **177**, 3275–3284.

29 T. Ishiyama, H. Kishimoto, K. D. - Bagarinao, K. Yamaji, T. Horita and H. Yokokawa, *ECS Trans.*, 2017, **78**, 321–326.

30 B. Butz, A. Lefarth, H. Störmer, A. Utz, E. Ivers-Tiffée and D. Gerthsen, *Solid State Ionics*, 2012, **214**, 37–44.

31 A. Morrissey, J. R. O'Brien and I. E. Reimanis, *Acta Mater.*, 2016, **105**, 84–93.

32 M. O. Zacate, L. Minervini, D. J. Bradfield, R. W. Grimes and K. E. Sickafus, *Solid State Ionics*, 2000, **128**, 243–254.

33 Y. Wang, C. Cai, L. Li, L. Yang, Y. Zhou and G. Zhou, *AIP Adv.*, 2016, **6**, 095113.

34 M. Kilo, G. Borchardt, B. Lesage, O. Katasov, S. Weber and S. Scherrer, *J. Eur. Ceram. Soc.*, 2000, **20**, 2069–2077.

35 C. Argirusis, M. A. Taylor, M. Kilo, G. Borchardt, F. Jomard, B. Lesage and O. Kaïtasov, *Phys. Chem. Chem. Phys.*, 2004, **6**, 3650–3653.

36 J. An, A. L. Koh, J. S. Park, R. Sinclair, T. M. Gür and F. B. Prinz, *J. Phys. Chem. Lett.*, 2013, **4**, 1156–1160.

37 J. An, J. S. Park, A. L. Koh, H. B. Lee, H. J. Jung, J. Schoonman, R. Sinclair, T. M. Gür and F. B. Prinz, *Sci. Rep.*, 2013, **3**, 2680.

38 X. J. Huang and W. Weppner, *J. Chem. Soc. Faraday. Trans.*, 1996, **92**, 2173–2178.

39 M. Yashima, M. Kakihana and M. Yoshimura, *Solid State Ionics*, 1996, **86–88**, 1131–1149.

40 C. Viazzi, J. P. Bonino, F. Ansart and A. Barnabé, *J. Alloys Compd.*, 2008, **452**, 377–383.

41 K. Develos-Bagarinao, T. Yamaguchi and H. Kishimoto, *Nanoscale*, 2023, **15**, 11569–11581.

42 H.-S. Noh, J.-W. Son, H. Lee, H.-S. Song, H.-W. Lee and J.-H. Lee, *J. Electrochem. Soc.*, 2009, **156**, B1484.

43 Y. Yang, Y. Zhang and M. Yan, *Sep. Purif. Technol.*, 2022, **298**, 121627.

44 S. K. Kim, H. J. Lee, J. Y. Moon, Y. R. Jo, J. Lee, J. H. Park, S. D. Kim and J. H. Joo, *J. Mater. Chem. A*, 2024, **12**, 8319–8330.